



Contents lists available at ScienceDirect

# Journal of Rock Mechanics and Geotechnical Engineering

journal homepage: [www.jrmge.cn](http://www.jrmge.cn)

## Full Length Article

# Simulation of dilatancy-controlled gas migration processes in saturated bentonite using a coupled multiphase flow and elastoplastic H<sup>2</sup>M model

Eike Radeisen<sup>a,\*</sup>, Hua Shao<sup>a</sup>, Jürgen Hesser<sup>a</sup>, Olaf Kolditz<sup>b,c</sup>, Wenjie Xu<sup>d</sup>, Wenqing Wang<sup>b</sup><sup>a</sup> Department of Rock Characterization for Storage and Final Disposal, Federal Institute for Geosciences and Natural Resources (BGR), Hannover, 30655, Germany<sup>b</sup> Department of Environmental Informatics, Helmholtz Center for Environmental Research (UFZ), Leipzig, 04341, Germany<sup>c</sup> Department of Applied Environmental Systems Analysis, Technische Universität Dresden, Dresden, 01069, Germany<sup>d</sup> Department of Civil Engineering and Architecture, Zhejiang University, Hangzhou, 310058, China

## ARTICLE INFO

### Article history:

Received 1 February 2022

Received in revised form

4 April 2022

Accepted 15 May 2022

Available online 17 June 2022

### Keywords:

H<sup>2</sup>M coupling

Gas migration

Dilatancy-controlled flow

Continuous approach

Geomaterial heterogeneity

OpenGeoSys

## ABSTRACT

Dilatancy-controlled gas flow in preferential pathways plays a key role in the safety analysis of radioactive waste repositories. This is particularly the case for bentonite, an often-preferred barrier material. Gas flow in preferential pathways is characterized by localization and spontaneous behavior, which is challenging to simulate in numerical models due to strong hydro-mechanical coupling. To analyze a laboratory experiment in the framework of the DECOVALEX-2023 project, this study introduced a new approach of combining continuous modelling methods with spatial material properties derived from material heterogeneities and experimental observations. The proposed model utilized hydro-mechanical spatial distributions, namely Young's modulus and gas entry pressure, and elastoplasticity combined with a linear swelling model. A conceptual strain-dependent permeability approach simulated dilatancy-controlled gas flow based on hydro-mechanical coupling. To test the effectiveness of the presented approach, a gas injection test in a compacted, saturated bentonite sample was simulated using the open-source code OpenGeoSys 5.8 and compared with experimental observations. The presented methodology is capable of simulating localized gas flow in preferential pathways. The spatial distributions of Young's modulus and gas entry pressure affect the swelling pressure, relative permeability and, in combination with the strain-dependent permeability model, also the intrinsic permeability.

© 2023 Institute of Rock and Soil Mechanics, Chinese Academy of Sciences. Production and hosting by Elsevier B.V. This is an open access article under the CC BY-NC-ND license (<http://creativecommons.org/licenses/by-nc-nd/4.0/>).

## 1. Introduction

In radioactive waste repositories, hydrogen and other gases are produced by the corrosion of metallic materials under anoxic conditions, the radioactive decay of waste, or the radiolysis of water (Cuss et al., 2012). A discrete gas phase is formed between metallic materials and surrounding repository rocks when gas production by one or more of these processes exceeds the flow processes and the solution capacity of the pore fluid. The initial flow processes are diffusion and advection of the dissolved gas within the pores of the surrounding geomaterials (Wikramaratna et al., 1993; Ortiz et al., 2002; Weetjens and Sillen, 2006). Significant amounts of gas can accumulate in argillaceous materials, where advection and

diffusion in the intrinsic porosity are very slow processes due to capillary restrictions (Aziz and Settari, 1979). Continuous gas production will steadily increase the gas pressure in the gas phase until a critical value, the gas entry pressure, is reached. The gas entry pressure is defined as the pressure limit for infiltration of the gas phase into the pore system of the fully saturated surrounding materials, where gas and pore water form a two-phase system. If the fluid pressure exceeds the dilatancy limit in the rock, dilatant pathways are formed (Marschall et al., 2005; Cuss et al., 2011; Harrington et al., 2012, 2014). The creation of dilatant pathways increases the permeability significantly, which enables the migration of the gas through argillaceous host rocks and clay-based engineered barriers. At high gas pressures, the integrity of the repository may be compromised by dilatancy or fracturing processes, and radioactive nuclides may enter the groundwater (NAGRA, 2002). Therefore, the quantification of gas evolution and dilatancy processes is of vital importance for the design of radioactive waste repositories to ensure the safety.

\* Corresponding author.

E-mail address: [eike.radeisen@bgr.de](mailto:eike.radeisen@bgr.de) (E. Radeisen).

Peer review under responsibility of Institute of Rock and Soil Mechanics, Chinese Academy of Sciences.

There is no universal method for modeling gas flow in clay and bentonite. Although, there are a growing number of numerical approaches as the scientific community becomes aware of the importance of this issue in the context of nuclear waste management (Bond and Birkholzer, 2020). Continuous two-phase hydro-mechanical (HM) coupled models without representation of fractures use constitutive relations to represent the effects of dilatancy, such as gas pressure dependent permeability (NAGRA, 2002; Senger et al., 2006; Xu et al., 2011) and deformation dependent permeability (Xu et al., 2013; Nguyen and Le, 2015). Gas pressure dependent permeability is often used in combination with a threshold pressure. Below this threshold, the influence of the gas pressure remains small, and the HM process is described by the change of volume in the pore space, with little influence on the permeability. Above the threshold, a sharp increase in permeability is simulated due to the connection and propagation of microcracks. The resulting flow processes are partly consistent with experimental data, but do not account for mechanical coupling as the basic pressure dependent permeability model is based on hydraulic properties only. As a result, the simulated gas outflow rate is not influenced by the mechanical regime. This calculated result differs from experimental observations, where gas outflow rates change with varying confining pressures (Popp et al., 2007). In contrast, the deformation-dependent permeability approach allows the coupling of mechanical and hydraulic effects.

Modified two-phase flow models consider HM-coupled fractures, which are assumed to behave as gas preferential pathways. These models represent physics more accurately but need additional information such as heterogeneous variability of material properties. Modified models without explicit representation of fractures may use embedded structures within plastic materials (Damians et al., 2020; Shovkun et al., 2020). Discrete representation of fracture generation in coupled H<sup>2</sup>M models (the two-phase HM-coupled models) may use a lattice approach (Asahina et al., 2014; Kim et al., 2021). The constitutive relations in H<sup>2</sup>M coupling of both approaches are created by combining matrix and fracture equations. Models using embedded fractures need less computational efficiency than discrete representations but incorporate only an indirect coupling process.

In this study, an empirical strain-dependent permeability approach by Xu et al. (2013) was extended with a dual heterogeneous material model, and was applied in a fully coupled two-phase numerical flow model with an elastoplastic continuum. Spatial distributions of gas entry pressure and Young's modulus were combined with constitutive relations such as a linear swelling model and Mualem-van Genuchten relative permeability. Combining this with a new approach for deriving material models from experimental data provided the basis for forming dilatant gas paths. A gas flow experiment by Daniels and Harrington (2017) was simulated to verify the approach. An investigation of the HM coupling provided further information regarding the applicability of the approach. The numerical simulation was performed with the numerical code OpenGeoSys (OGS).

## 2. Concept

### 2.1. Characteristics of clayey materials

Sub-microscopic dimensions of interparticle spaces and very large specific surface areas of the mineral phases (Liu et al., 2020) generally characterize materials containing clay (e.g. claystone and bentonite). This leads to strong chemical-physical interactions between water molecules and mineral surfaces and generally very low permeabilities (Graham et al., 2012), which makes it difficult to evaluate gas flow in clayey materials with conventional two-phase

models. The tensile strength is generally low and deformation of the grain matrix can be easily carried out (Donohew et al., 2000). At larger deformations, severe permeability changes can occur due to dilatancy. The creation of pathways is pressure-induced, and their aperture is a function of their internal gas pressure and structural constraints within the clay.

Gas entry and breakthrough are accompanied by the development of pathways propagating through the clay from the gas source to the sink (Horseman et al., 1999). Gas flow within clayey materials is mostly restricted to these pathways (Angeli et al., 2009; Cuss et al., 2011; Harrington et al., 2012, 2014). After pressure reduction, these pathways may close under continuous stress conditions. In case of a renewed pressure increase, the previously closed pathways can be reactivated at a lower pressure than initially needed. Claystone mostly possesses anisotropic rock properties due to its microscopical mineral structure and genesis. Clay-based engineered barriers such as bentonite are assumed to be homogeneously isotropic (Graham et al., 2012).

Zhang (2016) conducted a number of triaxial tests to investigate the stress-strain-permeability behavior of claystone during damage and recompression (Fig. 1). In these tests, the predominant process in the beginning is compression, represented by a decreasing volume of the sample. The compression in axial direction is denoted with a positive axial strain and initiated by an increasing axial stress  $\sigma_1$ . The flow process involves molecule diffusion and two-phase flow in the original porosity. Within one laboratory test with radial stress  $\sigma_3 = 1$  MPa, the change from compaction to extension of the sample starts approximately at a differential stress level of 23 MPa. Higher stresses cannot be further absorbed by the rock and a shear fracture occurs accompanied by a correspondingly increased permeability.

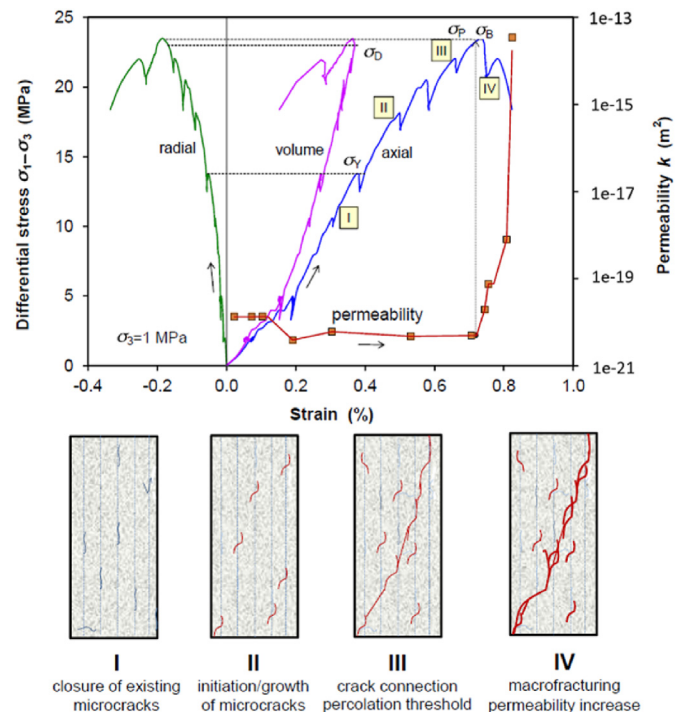


**Fig. 1.** Stress-strain-dependent permeability of claystone during damage and recompression in four stages: compressive stress state with closure of existing microcracks (I), initiation of microcracks (II), crack connection percolation threshold (III), and macrofracturing (IV) in a tensile stress state with permeability and sample volume increase, including thresholds of yield  $\sigma_Y$ , dilatancy  $\sigma_D$ , percolation  $\sigma_P$  and peak failure  $\sigma_B$  (after Zhang, 2016).

This experiment shows the strong correlation between strain and permeability as well as the exponential nature of this relationship. Volumetric strain is considered to cause the initial increase in permeability, while the sharp increase in permeability occurs with the onset of plastic deformation.

2.2. Model set-up

In this study, we used the measured HM values of a laboratory test previously conducted by Daniels and Harrington (2017) and presented in the DECOVALEX-2023 project (DECOVALEX, 2023) for comparison and validation of the numerical results. The gas flow experiment for the investigation of the breakthrough phase and decay behavior used helium as a steadily pressurizing gas phase. The test was conducted within a cylindrical (120 mm × 60 mm), pre-compacted, initially water-saturated MX-80 bentonite sample enclosed by a constant-volume container (Fig. 2).

The pressure container was instrumented with two axial and three radial load cells (LC 1–LC 3, LC backpressure, LC injection) to measure axial and radial stresses. Pore pressure was recorded by three radial arrays (PP A1–PP A3) with 12 pore pressure transducers arranged regularly around the circumference of the container. A 6.4 mm diameter steel tube, originally designed for a radial injection case, was inserted into the top of the sample.

The gas flow experiment was conducted for 120 d, with gas injection at the bottom and outflow observed at the top of the sample. The experimental data from the laboratory test was divided into 4 temporal sections (Fig. 3): a hydration phase accompanied by a quiescent phase (A–B), gas flow into system (B–D), gas breakthrough (C), gas peak pressure (D) and a decay phase (D–End). In the first 7.3 d, the sample is equilibrated with water from radial and backpressure filters (equilibration phase). After a sufficient swelling pressure is reached, the hydration phase is initiated and lasts for 32 d with an applied external pore pressure of 1 MPa, accompanied by the buildup of swelling pressure (Tamayo-Mas et al., 2021). At 39 d, the gas injection phase starts with a constant gas pressure of 3 MPa continuing for 7 d. Starting with 46 d, the injection pressure increases gradually with a gas compression rate of 500 μL/h (46–54 d) and 375 μL/h (54–71 d). Gas breakthrough (defined by the first measured gas efflux) occurs at 63.8 d with a gas breakthrough pressure of 10.5 MPa. After the breakthrough, the gas pressure decreases, while the gas compression pump still works. The gas injection pump stops on 71 d. The pore pressure decreases significantly after that.

An axisymmetric model with triangle elements was used for numerical simulation. The grid consists of 7084 elements and 3691

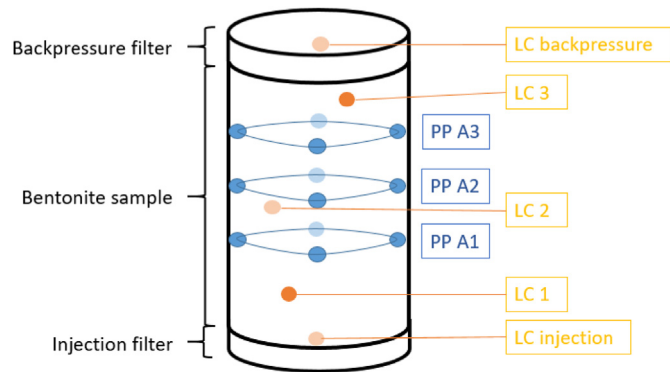


Fig. 2. Bentonite sample enclosed by a constant-volume container with 12 pore pressure (blue), two axial and three radial stress (orange) measuring devices (LC: load cell, PP: pore pressure measurement points) (after Daniels and Harrington, 2017).

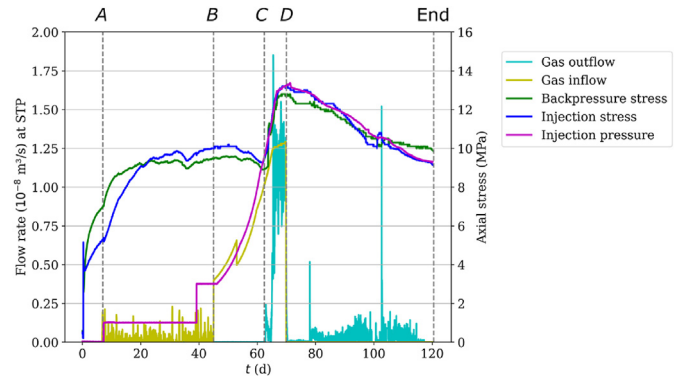


Fig. 3. Laboratory test results of a helium gas-induced bentonite sample, showing the gas flow rate into the system and outflow rate (averaged over approximately 6 h), injection pressure recorded in injection pump, as well as the measured injection and backpressure stress. An equilibrium phase (0–A) is followed by the hydration phase (A–B); the gas inflow into the system starts at point B and increases until reaching the breakthrough at point C; a short gas outflow event (C–D) is followed by the decay phase (D–End). Standard temperature and pressure (STP) are defined as 273.15 K, 101.325 kPa respectively. A detailed description of the experiment can be found in Daniels and Harrington (2017).

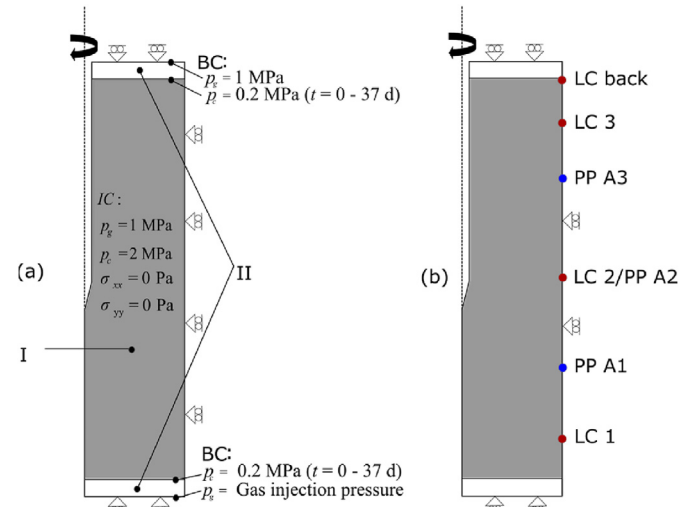


Fig. 4. (a) Axisymmetric model consisting of bentonite (I) and filter material (II) with initial conditions (IC) and boundary conditions (BC), and (b) the measuring points at the domain boundary. ( $\sigma_{xx}$ : Radial stress;  $\sigma_{yy}$ : Axial stress.)

nodes. A uniform spatially discretization was used in which the elements are approximately the same size over the entire model domain, with side lengths of 0.8–1.2 mm. The quality of the mesh elements is calculated based on the aspect ratio  $\zeta$  of the individual element. The lowest aspect ratio is 0.8, which is in an acceptable range of  $0.5 < \zeta < 1$  ( $\zeta$  is defined as the ratio of the shortest edge length to the longest edge length of the individual element). An algorithm with different time increments was used. At the beginning of the simulation (0–55 d), the minimum time increment is 100 s and the maximum time increment is 3000 s. The step size is reduced to 60 s during breakthrough and for the decay phase. The simulation starts on 0 d and lasts for 120 d. Quadratic orders of approximation were used for the mechanical processes, and linear approximation for the hydraulic processes.

The model consists of two materials (Fig. 4a): the bentonite sample (properties are listed in Table 1) and a filter at the bottom and top of the model with a high permeability ( $k = 1 \times 10^{-14} \text{ m}^2$ ) and a high Young’s modulus ( $E = 200 \text{ GPa}$ ). Boundary conditions for

**Table 1**  
Material properties for the MX-80 bentonite sample and fluid properties.

Mechanical parameter	Symbol	Value	Unit
Angle of internal friction	$\varphi$	21	°
Biot coefficient	$\alpha$	0.9	–
Cohesion	$c$	1.2	MPa
Density of solid grains	$\rho_s$	$2.45 \times 10^3$	kg/m <sup>3</sup>
Dilatancy angle	$\psi$	21	°
Maximum swelling stress	$\sigma_{\max}^{sw}$	10	MPa
Poisson's ratio	$\nu$	0.35	–
Porosity	$\phi$	0.44	–
Tensile strength	$f_t$	0.8	MPa
Mean Young's modulus	$\bar{E}$	0.307	GPa
Minimum Young's modulus	$E_{\min}$	0.207	GPa
Maximum Young's modulus	$E_{\max}$	0.407	GPa
Hydraulic parameter			
Gas (helium) density at STP	$\rho_g$	0.1786	kg/m <sup>3</sup>
Gas (helium) dynamic viscosity	$\mu_g$	$1.9 \times 10^{-5}$	kg/m/s
Initial intrinsic permeability	$k_0^{\text{int}}$	$3 \times 10^{-21}$	m <sup>2</sup>
Maximum degree of saturation	$S_{\max}$	0.99	–
Relative permeability water	$k_w^r$	van-Genuchten	m <sup>2</sup>
Relative permeability gas	$k_g^r$	van-Genuchten	m <sup>2</sup>
Residual degree of saturation	$S_{\text{res}}$	0.01	–
Tortuosity	$\tau$	1	–
Water density	$\rho_w$	$1 \times 10^3$	kg/m <sup>3</sup>
Water dynamic viscosity	$\mu_w$	$1 \times 10^{-3}$	kg/m/s
van Genuchten parameter			
Mean gas entry pressure	$p_{g, \text{entry}}$	10.5	MPa
Minimum gas entry pressure	$p_{g, \text{entry, min}}$	9.5	MPa
Maximum gas entry pressure	$p_{g, \text{entry, max}}$	11.8	MPa
van Genuchten parameter	$m$	2	–

each outline are defined to have no displacement in the perpendicular direction and no fluid flow, except for the injection hole and the outflow polyline for which Dirichlet boundary conditions are defined for capillary and gas pressures. The hydration of the sample with a low capillary pressure ( $p_c = 0.2$  MPa) at the upper and lower boundaries of the sample was carried out over a period of 37 d. The gas pressure (backpressure) at the outflow boundary is constant at  $p_g = 1$  MPa. The gas pressure at the gas injection was applied with the measured data of the laboratory experiment (Fig. 3). Temperature is constant at 20 °C throughout the simulation. Material properties and initial conditions were measured by Daniels and Harrington (2017) and summarized in Tamayo-Mas et al. (2021). The measuring points around the cylinder in the experiment were arranged at the outer edge at the corresponding heights in the numerical model (Fig. 4b).

### 2.3. Heterogeneity

Heterogeneous distributions of material properties provide a mechanism by which gas flow can create preferential pathways in bentonite. This material dependence has been observed in both laboratory experiments and large-scale in situ experiments. Brú and Pastor (2006) and Rawat et al. (2020) demonstrated that microscale heterogeneity of the pore space and dry density is important for fluid flow predictions in artificial small-scale bentonite samples. The same was observed in a large-scale in situ experiment. The FEBEX project conducted a large-scale experiment with a bentonite barrier. It is observed that significant water content and dry density gradients are present throughout the barrier after 18 years of operation (Villar et al., 2020). Based on these findings, spatially uniform distributions of material HM properties were implemented in the numerical code. Young's modulus is selected to characterize the heterogeneous distribution of the dry density. The gas entry pressure is selected to representing both the spatially distributed water saturations and the dry density in the sample. Similar approaches were developed by Guo and Fall (2019)

for Young's modulus, critical tensile stress and intrinsic permeability, and by Damians et al. (2020) for intrinsic permeability and retention curve.

The material properties of the gas entry pressure and Young's modulus are described by a probability density function  $p(x)$  of uniform distribution:

$$p(x) = \frac{1}{b_{\max} - b_{\min}} \quad (1)$$

where  $b_{\max}$  and  $b_{\min}$  are the maximum and minimum values of the corresponding material property, respectively.

The capillary pressure of the maximum pore throat determines the value of the gas entry pressure. By applying van Genuchten's law for two-phase flow, the gas entry pressure is related to the water saturation in the pores. In analyzing the measurements of Daniels and Harrington (2017), two points of interest can be identified. The first point locates the first gas outflow after 62.4 d of the experiment. The corresponding gas injection pressure is 9.5 MPa (Fig. 5) and represents the minimum gas entry pressure for the spatial distribution. Since it is not possible with the available data to distinguish between breakthrough pressure and entry pressure, they are equated here. The second point of interest is where the largest increase in gas outflow rate is measured. We assume that this indicates the maximum gas entry pressure for the spatial distribution. This is the case after 65.4 d of the experiment, with a corresponding injection pressure of 11.8 MPa. The spatial distribution of Young's modulus is derived from a similar modelling approach conducted by Damians et al. (2020).

### 3. Numerical fundamentals

The numerical simulation of the coupled two-phase flow and mechanical process within the bentonite sample was performed using the OGS v. 5.8 code (Wang et al., 2021). OGS is based on an object-oriented finite element method (FEM) and has been developed as an open-source initiative since the mid-1980s for numerical simulations of thermo-hydro-mechano-chemical processes in porous and fractured media (Kolditz et al., 2012). Capillary pressure ( $p_c$ ), gas pressure ( $p_g$ ) and solid displacement ( $\mathbf{u}$ ) are primary quantities in the H<sup>2</sup>M model. The relevant stress measure is the

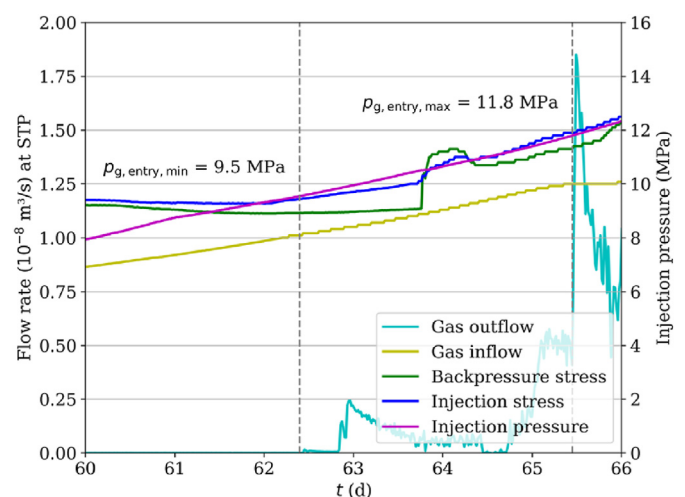


**Fig. 5.** Measurements of the gas flow experiment between 60 d and 66 d. The first measured gas outflow and the highest increase are marked with a dashed line in grey and labelled with the corresponding value of the injection pressure. The values represent the minimum and maximum gas entry pressure.

Cauchy stress tensor  $\sigma$ , and the relevant strain measure is the small-strain tensor  $\epsilon$  (Kolditz et al., 2012). The basic HM analysis in a quasi-static small-strain setting was performed by using local partial differential equations (PDE) forms of the equilibrium conditions.

In this study, the mass balance and momentum balance equations were solved monolithically in the model, with a fully implicit backward Euler scheme for the temporal integration. The biconjugate gradient stabilized method (BiCGSTAB) was used as a linear solver with an overall tolerance of  $10^{-15}$ . Picard fixed point iterations were used as a nonlinear solver with a relative tolerance of  $10^{-4}$ .

### 3.1. Constitutive relations

The two-phase flow consists of an assumed incompressible liquid phase (water, denoted by  $w$ ) and a compressible gas phase (helium, denoted by  $g$ ).

#### 3.1.1. Hydraulic process

The hydraulic processes are based on the primary variables of capillary pressure and gas pressure. Water pressure ( $p_w$ ) is calculated with the primary variables for a two-phase system of a representative elementary volume (REV) by

$$p_w = p_g - p_c \quad (2)$$

Eq. (2) can be used to simplify the calculation for pore pressure ( $p_p$ ), based on  $S_w + S_g = 1$  as follows:

$$p_p = S_g p_g + S_w p_w = p_g - S_w p_c \quad (3)$$

where  $S_w$  is the water saturation and  $S_g$  is the gas saturation.

Capillary pressure and relative permeability are further characterized using the Mualem-van Genuchten analytical functions, which are based on soil water retention curves. The capillary pressure is defined by the van Genuchten model (van Genuchten, 1980) and hence we have

$$p_c = p_{g, \text{entry}} \left( S_{ec}^{\frac{m}{1-m}} - 1 \right)^{\frac{1}{m}} \quad (4)$$

where  $m$  is a material parameter,  $S_{ec} = (S_w - S_{res}) / (S_{max} - S_{res})$  is the effective saturation and  $p_{g, \text{entry}}$  is the gas entry pressure, a time-independent parameter with spatial differences. By applying the van Genuchten model for two-phase flow, the gas entry pressure is directly linked to the water saturation in each element. Due to the spatial differences in the gas entry pressure, the water saturation is similarly distributed. The unsaturated hydraulic conductivity is defined by the Mualem analytical function (Mualem, 1976) for water and gas as follows:

$$k_w^r = S_{ec}^{\frac{1}{2}} \left[ 1 - \left( S_{ec}^{\frac{m}{1-m}} - 1 \right)^2 \right] \quad (5)$$

$$k_g^r = (1 - S_{ec})^{\frac{1}{2}} \left( 1 - S_{ec}^{\frac{m}{1-m}} \right)^2 \left( 1 - \frac{1}{m} \right) \quad (6)$$

It is assumed that the water in the bentonite sample is absorbed by the clay minerals and that no free water phase is available after the hydration is completed. This behavior has been observed in some studies (Liu et al., 2014; Cui, 2017).

A deformation-dependent permeability approach is assumed in this study, linking dilatancy directly with permeability, which was first applied by Xu et al. (2013). The approach describes

permeability as a function of confining stresses. Without deformation, the permeability of the model is calculated using the intrinsic permeability multiplied by the relative permeabilities of water and gas, respectively. If deformation occurs, the volumetric strain ( $\epsilon_{vol}$ ) and the equivalent plastic strain ( $\bar{\epsilon}_{pl}$ ) integrated in the model influence the permeability as follows:

$$\mathbf{k}^{\text{int}} = f(\Delta\epsilon_{vol}) e^{b_1 \Delta\bar{\epsilon}_{pl}} k_0^{\text{int}} \mathbf{I} \quad (7)$$

where

$$f(\Delta\epsilon_{vol}) = \begin{cases} -10^{b_2 \Delta\epsilon_{vol}} & (\text{compaction}) \\ 10^{b_3 \Delta\epsilon_{vol}} & (\text{extension}) \end{cases} \quad (8)$$

where  $\mathbf{I}$  is the identity tensor,  $k_0^{\text{int}}$  and  $\mathbf{k}^{\text{int}}$  are the initial intrinsic permeability and the intrinsic permeability, respectively; and  $b_1$ ,  $b_2$  and  $b_3$  are empirical variables. Different parameters were used for compaction and extension following observations in laboratory experiments (Zhang, 2016). The approach is similar to porosity-controlled permeability approaches (Zhu and Wei, 2011; Senger et al., 2014, 2018). The advantage of this strain-dependent permeability approach is that not only volumetric strain but also plastic strain is used, which gives the model an additional degree of freedom for calibration. The strong dependency of the permeability on plastic strain (Fig. 6) displays the behavior demonstrated in the laboratory experiment by Zhang (2016) as shown in Fig. 1. An upper limit of the permeability increase is defined by three orders of the magnitude (Xu et al., 2013) for both volumetric and plastic deformation, which refers to previous laboratory tests (Xu et al., 2011).

For calibration of the approach to the experimental data set, five different pairs of values were utilized for the parameters  $b_1$  and  $b_3$ . The parameter  $b_3$ , relevant for the influence of volumetric strain, is increased stepwise in five steps from 100 to 500. The parameter  $b_1$ , relevant for the influence of plastic strain, corresponds to 2 times the respective value of  $b_3$ .

Considering the water pressure, relative permeability for water and gas, and the strain-dependent permeability, the flux  $\mathbf{q}_\xi$  of both fluid phases  $\xi = w, g$  is calculated by the modified Darcy's law (Darcy, 1856) as follows:

$$\mathbf{q}_\xi = -\rho_\xi \frac{k_\xi^r}{\mu_\xi} (\nabla p_\xi - \rho_\xi \mathbf{g}) \quad (9)$$

where  $\nabla$  is the Nabla operator,  $\mathbf{k}^{\text{int}}$  is the intrinsic permeability,  $k_\xi^r$  is the relative permeability of the corresponding specific phase,  $\rho_\xi$  is the fluid density of the corresponding phase,  $\mu_\xi$  is the fluid viscosity of the corresponding phase and  $\mathbf{g}$  is the gravitational acceleration.

#### 3.1.2. Mechanical process

A deformable bentonite matrix based on elastoplasticity is considered in the coupled H<sup>2</sup>M model. After Terzaghi (1936), the effective stress  $\sigma'$  is derived from the total stress  $\sigma$ , negative in compression, and the pore-pressure  $p_p$  with following relation:

$$\sigma' = \sigma + p_p \mathbf{I} \quad (10)$$

With the introduction of pore-fluids under pressure in porous solids, stress-strain effects and physical properties calculated by numerical simulations are more consistent with experimental observations. However, the compressibility of clay due to its high porosity and the shape of clay minerals requires an effective stress law (Biot, 1941) in which a partial transmission of pore-pressure to the granular matrix is modified with an effective pressure coefficient (Biot's coefficient)  $\alpha$ :

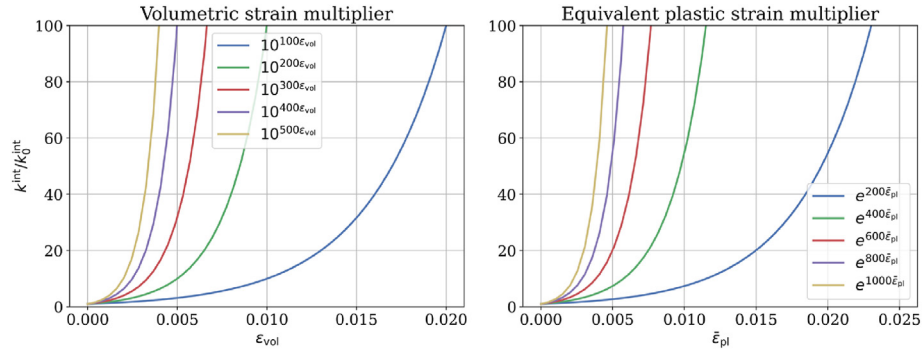


Fig. 6. Volumetric and equivalent plastic strain-dependent permeability factor according to Eqs. (7) and (8) for selected cases.

$$\boldsymbol{\sigma}' = \boldsymbol{\sigma} + \alpha p_p \mathbf{I} \quad (11)$$

The swelling stress of the bentonite is based on the linear swelling model proposed by Rutqvist et al. (2011) which defines the increment of swelling stress  $\Delta \boldsymbol{\sigma}^{sw}$  to be proportional to liquid saturation increment. By simplifying the parameters of the original formula and introducing a constraint to eliminate shrinkage stress when saturation is below initial saturation, the swelling model takes the form:

$$\Delta \boldsymbol{\sigma}^{sw} = \beta \Delta S_w \mathbf{I}, \quad \forall S_w \in [S_{res}, S_{max}] \quad (12)$$

where  $\beta = \sigma_{max}^{sw} / (S_{max} - S_{res})$  is a swelling coefficient that depends on the maximum swelling stress  $\sigma_{max}^{sw}$ .

### 3.2. Balance equations

Applying a continuum as the model environment allows the use of established physical conservation laws where fundamental properties such as mass, momentum, and energy are preserved throughout the system.

#### 3.2.1. Momentum balance equation

In a domain that considers a two-phase model within a porous solid, the effective stress law Eq. (10) and Cauchy stress tensor formulate the linear momentum balance equation (Kolditz et al., 2012), using the pore pressure expression Eq. (2) considering the primary variables of capillary pressure and gas pressure:

$$\nabla \left[ \boldsymbol{\sigma}' - \alpha (p_g - S_w p_c) \mathbf{I} \right] + \rho \mathbf{g} = \mathbf{0} \quad (13)$$

#### 3.2.2. Mass balance equation

In this isothermal two-phase flow process, the partially saturated sample is treated as an immiscible two-phase system. Based on the modified Darcy law Eq. (8), the balance equation for mass conservation of the liquid phase can be derived. In the representation depending on the primary variables (Kolditz et al., 2018), the equation is expressed as follows:

$$\begin{aligned} & \phi \rho_w \frac{\partial S_w}{\partial p_c} \dot{p}_c + \phi \rho_w S_w \nabla \cdot \mathbf{u} \\ & + \nabla \cdot \left[ \rho_w \frac{\mathbf{k}^{int} k_w^r}{\mu_w} \left( -\nabla p_g + \nabla p_c + \rho_w \mathbf{g} \right) \right] = Q_w \end{aligned} \quad (14)$$

where  $\phi$  is the porosity,  $\dot{p}_c = dp_c/dt$  is the temporal derivative of the capillary pressure,  $\dot{\mathbf{u}} = d\mathbf{u}/dt$  is the temporal derivative of the

displacement vector and  $Q_w$  represents the water source and sink term. Similarly, the mass balance equation of the gas phase is expressed as follows:

$$\begin{aligned} & -\phi \rho_g \frac{\partial S_w}{\partial p_c} \dot{p}_c + \phi \rho_g (1 - S_w) \nabla \cdot \mathbf{u} + \phi (1 - S_w) \left( \frac{\partial \rho_g}{\partial p_g} \dot{p}_g + \frac{\partial \rho_g}{\partial p_c} \dot{p}_c \right) \\ & + \nabla \cdot \left[ \rho_g \frac{\mathbf{k}^{int} k_g^r}{\mu_g} \left( -\nabla p_g + \rho_g \mathbf{g} \right) \right] = Q_g \end{aligned} \quad (15)$$

where  $\dot{p}_g = dp_g/dt$  is the temporal derivative of the gas pressure and  $Q_g$  represents the source and sink term of the gas. The gas is assumed to behave as an ideal gas with the density described by the ideal gas law  $\rho_g = \frac{p_g M_g}{RT}$  ( $M_g$  is the molar mass of the gas phase,  $R$  is the ideal gas constant), neglecting phase transitions as well as dissolved gas in the liquid phase and water vapor in the gas phase. These assumptions are plausible as the aforementioned processes have only a minor influence compared to dilatancy-controlled advective gas transport under high gas pressure gradients.

### 3.3. Drucker-Prager criterion

The mechanical behavior of the solid matrix is assumed elastoplastic. The strain tensor is composed of two constitutive parts, the elastic tensor  $\boldsymbol{\epsilon}_{el}$  and the partial plastic strain tensor  $\boldsymbol{\epsilon}_{pl}$ . A mathematically ascertainable functional relationship between stress rate and the elastic strain rate is created by:

$$\dot{\boldsymbol{\sigma}} = \mathbb{C} \dot{\boldsymbol{\epsilon}}_{el} \quad (16)$$

where  $\dot{\boldsymbol{\sigma}}$  is the stress rate tensor,  $\mathbb{C}$  is a fourth order material tensor and  $\dot{\boldsymbol{\epsilon}}_{el}$  is the elastic strain rate tensor. The partial plastic strain tensor is mathematically characterized based on so-called yield conditions  $\Phi_{pl}(\boldsymbol{\sigma})$ . The plastic strain rate tensor is defined based on the yield condition as follows:

$$\dot{\boldsymbol{\epsilon}}_{pl} = \lambda_{pl} \frac{\partial \Phi_{pl}(\boldsymbol{\sigma})}{\partial \boldsymbol{\sigma}} \quad (17)$$

where  $\lambda_{pl}$  is the so-called plastic multiplier.

The Drucker-Prager (DP) failure function was used to determine the yield condition (Drucker and Prager, 1952). The DP failure criterion established as a generalization of the von Mises yield criterion and, with its simple implementation and smooth failure function, offered an advantage for numerical analysis purposes (Wojciechowski, 2018).

$$\Phi_{pl}(\sigma) = \sqrt{J_2} + I_1 - \lambda \tag{18a}$$

$$J_2 = \frac{1}{2} \text{tr}(\sigma_d^2) \tag{18b}$$

$$I_1 = \text{tr}(\sigma) \tag{18c}$$

$$\sigma_d = \sigma - \frac{1}{3} \text{tr}(\sigma) \mathbf{I} \tag{18d}$$

where  $l$  and  $\lambda$  are material constants,  $J_2$  is the second invariant of the stress deviator tensor, with  $\sigma_d$  as deviatoric stress, and  $I_1$  is the first invariant of the Cauchy stress tensor. The material constants  $l$  and  $\lambda$  are derived from friction angle ( $\varphi$ ) and cohesion ( $c$ ) as follows:

$$l = \frac{2 \sin \varphi}{\sqrt{3}(3 - \sin \varphi)} \tag{19a}$$

$$\lambda = \frac{6c \cos \varphi}{\sqrt{3}(3 - \sin \varphi)} \tag{19b}$$

The DP criterion was modified to approximate the short-term laboratory strength of low-porosity rocks (Alejano and Bobet, 2012). A cap model was added that allows yield under hydrostatic pressure and tension cut off:

$$\Phi_{pl}(\sigma) = \sqrt{J_2 + \frac{1}{2} \alpha_p I_1^2} + I_1 - \lambda \tag{20}$$

with a plastic flow parameter  $\alpha_p = 0.1$  controlling a smooth tension cap. The smooth regularization of the yield surface in all stress states improves convergence of the stress-return algorithm, without changing the strength envelope.

## 4. Results

### 4.1. Calibration and comparison

The calibration of the strain-dependent permeability method was performed with five different pairs of values of the parameters  $b_1$  and  $b_3$ , where  $b_1$  is always twice the value of  $b_3$ . These pairs of values are described by the value of  $b_3$ , the parameter for the influence of the volumetric strain. A good agreement for the total outflow gas volume and a similar pattern of the gas outflow rate is

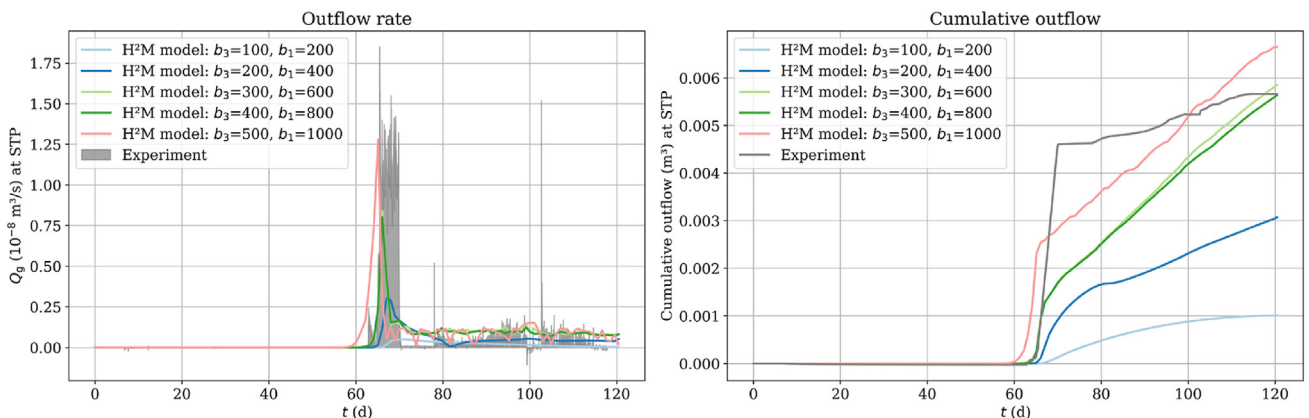


Fig. 7. Gas outflow rate (a) and cumulative outflow (b) of different models with varying parameter  $b_1$  and  $b_3$  of the strain-dependent permeability approach according to Eq. (7).

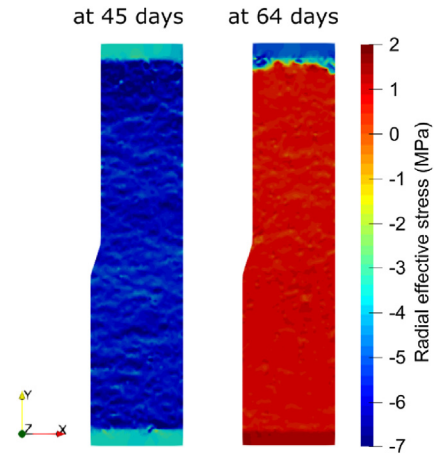
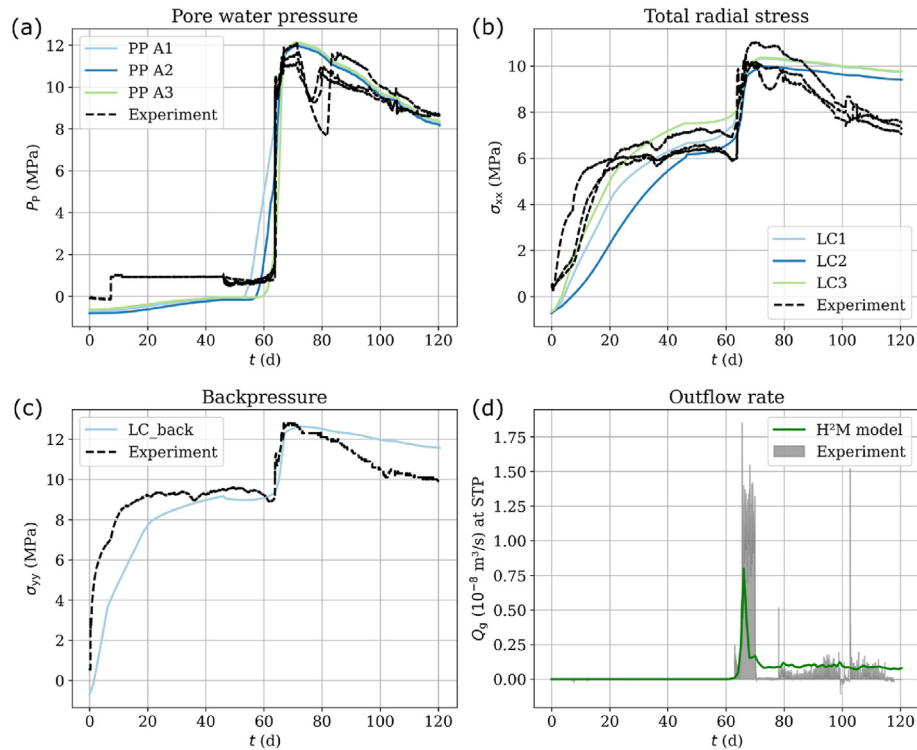


Fig. 8. Radial effective stress at the beginning of gas inflow (45 d) and after breakthrough (64 d). The stress state of the entire bentonite sample has changed from compressive to tensile after breakthrough.

important for a good fit of the parameters. The outflow rate of the H<sup>2</sup>M model is calculated at the boundary between the bentonite sample and the filter. All feature comparisons are depicted in Fig. 7. Two pairs of values ( $b_3 = 100$  and  $b_3 = 200$ ) underestimate the gas outflow in terms of rate, magnitude and temporal shape and one overestimates them ( $b_3 = 500$ ). The H<sup>2</sup>M models  $b_3 = 300$  and  $b_3 = 400$  have a similar shape of the rate over time and the best agreement with the breakthrough flow rate.

It can be observed that with increasing values of the strain-dependent permeability method, the maximum gas outflow rate and the total outflow increase. The peak outflow rate occurs earlier with increasing  $b_1$  and  $b_3$ . Since the pairs of values shown here record both lower and higher total outflows and show earlier as well as later peak gas flow rates, it can be assumed that the optimal pair of values for this model is in the indicated range. Better agreement can only be achieved by calibrating other material parameters or changing of the numerical method. To prove the concept of using material heterogeneity for dilatancy controlled pathways, the obtained agreement is sufficient. For this reason, the H<sup>2</sup>M model with parameter values  $b_1 = 800$  and  $b_3 = 400$  is selected for further investigation, due to the highest agreement of total outflow volume with the experimental data (Fig. 7b). Analysis of the stress distribution in the model before and after gas breakthrough shows how the stress state transitions from a compressed



**Fig. 9.** Comparison between measured and simulated values: (a) pore pressure in the radial arrays, (b) radial stress at load cells LC 1 (close to injection end), LC 2 (midplane lengthways) and LC 3 (close to backpressure end), (c) axial stress at the backpressure end-closure, and (d) gas outflow rate. Experimental data are from Daniels and Harrington (2017).

state to a state under tension (Fig. 8). This process is also observed in laboratory tests, as shown in Fig. 1, among others.

The comparison between numerical results and experimental measurements is presented in Fig. 9. The buildup of swelling pressure is slower in the numerical model than in the experiment, but after about 45 d, when full saturation ( $S_w > 98\%$ ) is reached, the calculated stresses agree well with the measured stresses. Gas injection into the system begins on 46 d with a Dirichlet boundary condition for gas pressure provided by the experimental set-up (Fig. 3). Breakthrough occurs between 60 d and 63 d, when the gas pressure in the injector system exceeds the gas entry pressure of the bentonite at 10.5 MPa and a steep increase in pore pressure and stress in the bentonite is measured. The pore pressure of the numerical model does not increase as spontaneously as in the experiment (Fig. 9a), but it agrees well with the maximum value and the decline after breakthrough. The total radial (Fig. 9b) and axial (Fig. 9c) stresses increase abruptly during gas breakthrough, derived from the increase in pore water pressure.

The differences between the measured and calculated pore pressure are relatively small (1%–5%) after breakthrough, except for the pressure drop observed in the laboratory experiment between 75 d and 80 d. The measured and calculated radial stresses have larger errors. While an average error of about 10% is calculated of all radial stresses at the breakthrough, the error increases gradually to about 40% at 120 d. The calculated axial stress agrees well with the measured axial stress during breakthrough, but the difference increases to an overall error of 18%.

Decreasing pore pressures for all three arrays and a small drop in radial stress in LC 3 were measured after peak gas pressure. This pressure loss and fall of radial stresses are not consistent with the numerical results, where a linear decrease without major drops is calculated. After a few days, the measured pore pressure increases, and the calculated results are again in good

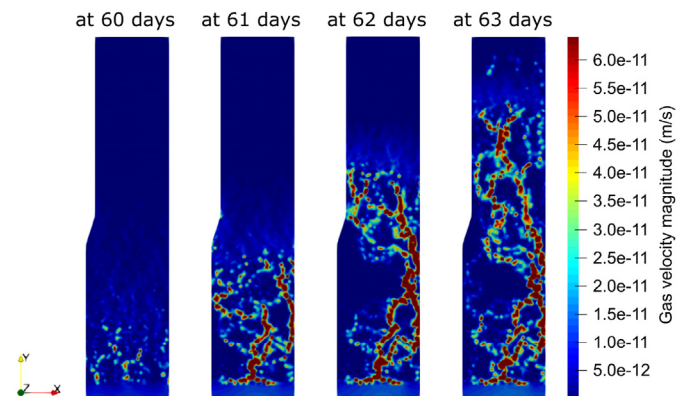


**Fig. 10.** Evolution of gas flow until breakthrough (duration of 60–63 d). The influence of the heterogeneity of the gas entry pressure is evident at the gas flow front, while the heterogeneity of the Young's modulus produces path-like flow patterns.

agreement with the experimental data. It is not conclusively clear what causes this short-term drop in the experimental data. A plausible explanation is the heterogeneity of the material and the geometry of the major gas preferential path has changed for a short time.

The gas breakthrough develops in the simulation between 60 d and 63 d. In the contour plot of the magnitude of the gas velocity vector (Fig. 10), the development of the flow path can be observed. It is apparent that the front of the gas flow consists of a diffuse area with slightly increased velocities. These areas are formed by the small differences in gas entry pressure between the mesh elements. In the area closer to the inflow filter, a stronger localization of the flow and higher gradual differences in velocity can be observed. These are produced by localized higher strains based on the

heterogeneous distribution of the Young’s modulus and the strain-dependent permeability model.

Despite good agreement in axial and radial stress between experimental data and calculated values, the applied HM coupled processes are not sufficient to achieve the very high spontaneous gas outflow for an extended period. Only a short gas outflow event with a high gas volume that is not stable for a longer time is achieved (Fig. 9d). A reason for the low stability of the gas outflow may be the consistently high water saturation and the consequently high swelling pressure (Fig. 9b). Since the flow is highly localized (Fig. 10), a small reduction in strain is sufficient to significantly reduce the permeability. Differences between the numerical model and experimental measurements may be due to time-dependent mechanical deformation models, which are not applied here.

4.2. Effects on relative and intrinsic permeability

Analyses of the effects of Young’s modulus and gas entry pressure on the gas flow regime show that both are important for localizing and increasing gas flow. The spatial distribution of the gas entry pressure and the water saturation has two effects on the flow regime:

- (a) Spatially distributed relative gas permeability based on the Mualem-van Genuchten law in Eq. (5), and
- (b) Spatially distributed swelling pressure based on the constitutive equation of linear swelling in Eq. (11).

The water saturation (Fig. 11a) after the hydration phase shows some small differences ( $S_w = 98\%–99\%$ ) which has significant effects on the relative gas permeability (Fig. 11b) due to the exponential relation. The effective stress in radial and axial direction (Fig. 11c and d) has strong gradients perpendicular to the respective stress direction but is relatively uniform in the stress direction. The effect of the swelling pressure on the gas flow cannot be quantified but is certainly affecting the strain and thus the intrinsic permeability. The swelling pressure and the spatial distribution of Young’s modulus affect the strain development, which affects the intrinsic permeability in turn (Fig. 12b), in combination with the strain-dependent permeability, which can be as high as a factor of  $10^6$ . The total permeability tensor for the gas phase calculated with  $\mathbf{k} = 10^{400\Delta\epsilon_{vol}} e^{800\Delta\epsilon_{pl}} k_g^r k_0^{int} \mathbf{I}$  is presented in Fig. 12c. The resulting gas velocity is presented in Fig. 12d. The magnitude of the gas velocity vector is relatively small during breakthrough, compared to the magnitude of the velocity vector after breakthrough, where it is 300 times larger.

5. Conclusions

The objective of this study is to generate dilatancy-induced areas of increased intrinsic permeability and their coalescence by permanently increasing the gas pressure in the system until gas flow along preferential pathways occurs. For this, a coupled two-phase flow and elastoplastic model was used with a strain-dependent permeability approach, enhanced with a dual heterogeneous distribution of Young’s modulus and gas entry pressure.

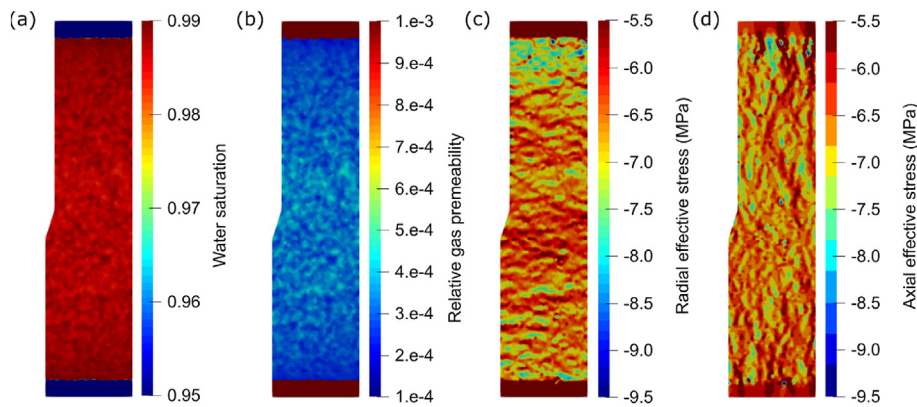


Fig. 11. (a) Water saturation, (b) relative gas permeability, (c) radial effective stress, and (d) axial effective stress at 45 d of the simulation (beginning of gas injection).

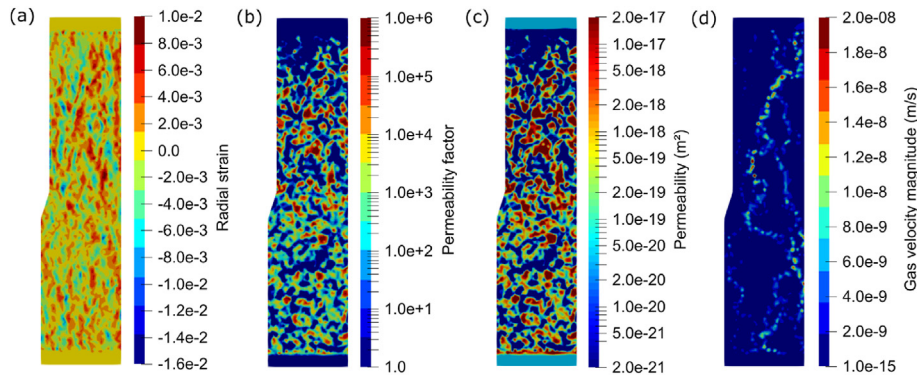


Fig. 12. (a) Radial strain, (b) permeability factor by the strain-dependent permeability method, (c) total permeability, and (d) gas velocity at 64 d of the simulation (after breakthrough).

Verification was performed by analyzing the experiment of Daniels and Harrington (2017). The results can be summarized as follows:

- (1) Essential features of a dilatancy-controlled flow can be reproduced with the presented approach, e.g. spontaneous and localized gas flow. The measured time series of the laboratory experiment can be roughly recalculated numerically with error deviations of up to 40%. Main features of the experiment like breakthrough time, maximum pressure and stress were well reproduced. Other features such as the temporal variation of the gas outflow rate and the stress decay after breakthrough were not well captured.
- (2) The creation of preferential pathways is successful. The predetermined heterogeneous distribution of the two material properties resulted in creation of the narrow areas of increased permeability extending from the gas inflow filter to the outflow filter.

Qualitative verification of the applicability of the presented approach for replication of laboratory results is successful. The calibration of strain-dependent permeability parameters shows a rough optimization. In future work, the selection of parameters needs to be improved with respect to the relationship between the parameters. The researches regarding spatial distributions, material heterogeneity and mesh dependency of spatially distributions should also be conducted.

#### Declaration of competing interest

The authors declare that they have no known competing financial interests or personal relationships that could have appeared to influence the work reported in this paper.

#### Acknowledgement

This research was conducted within the DECOVALEX-2023 project. DECOVALEX is an international research project comprising participants from industry, government, and academia, focusing on development of understanding, models and codes in complex coupled problems in sub-surface geological and engineering applications. DECOVALEX-2023 is the current phase of the project. The authors appreciate the DECOVALEX-2023 Funding Organisations Andra, BASE, BGE, BGR, CAS, CNSC, COVRA, US DOE, ENRESA, ENSI, JAEA, KAERI, NWMO, RWM, SÚRAO, SSM and Tai-power for their financial and technical support of the work described in this paper. The statements made in the paper are, however, solely those of the authors and do not necessarily reflect those of the Funding Organisations.

This work was further supported by the German Federal Ministry for Economic Affairs and Climate Action (BMWK).

#### References

- Alejano, L.R., Bobet, A., 2012. Drucker–prager criterion. *Rock Mech. Rock Eng.* 45 (6), 995–999.
- Angeli, M., Soldal, M., Skurtveit, E., Aker, E., 2009. Experimental percolation of supercritical CO<sub>2</sub> through a caprock. *Energy Proc.* 1, 3351–3358.
- Asahina, D., Houseworth, J.E., Birkholzer, J.T., Rutqvist, J., Bolander, J.E., 2014. Hydro-mechanical model for wetting/drying and fracture development in geomaterials. *Comput. Geosci.* 65, 13–23.
- Aziz, K., Settari, A., 1979. *Petroleum Reservoir Simulation*. Applied Science Publishers, London, UK.
- Biot, M.A., 1941. General theory of three-dimensional consolidation. *J. Appl. Phys.* 12, 155–164.
- Bond, A.E., Birkholzer, J.T., 2020. DECOVALEX-2019 Executive Summary. Lawrence Berkeley National Laboratory, Berkeley, USA.
- Brú, A., Pastor, J.M., 2006. Experimental characterization of hydration and pinning in bentonite clay, a swelling, heterogeneous, porous medium. *Geoderma* 134 (3–4), 295–305.
- Cui, Y.J., 2017. On the hydro-mechanical behaviour of MX80 bentonite-based materials. *J. Rock Mech. Geotech. Eng.* 9 (3), 565–574.
- Cuss, R.J., Harrington, J.F., Noy, D.J., 2012. Final Report of FORGE WP4.1.1: the Stress Path Permeability Experiment Conducted on Callovo-Oxfordian Claystone. British Geological Survey Commissioned Report. Report, No. CR/12/140. Nottingham, UK, p. 116.
- Cuss, R.J., Harrington, J.F., Noy, D.J., Wikman, A., Sellin, P., 2011. Large scale gas injection test (Lasgit): results from two gas injection tests. *Phys. Chem. Earth* 36 (17–18), 1729–1742.
- Damians, I.P., Olivella, S., Gens, A., 2020. Modelling gas flow in clay materials incorporating material heterogeneity and embedded fractures. *Int. J. Rock Mech. Min. Sci.* 136, 104524.
- Daniels, K.A., Harrington, J.F., 2017. The Response of Compact Bentonite during a 1D Gas Flow Test. British Geological Survey Open Report No. OR/17/067, Nottingham, UK, p. 19.
- Darcy, H., 1856. *Les fontaines publiques de la ville de Dijon: exposition et application*. Victor, Dalmont, Paris, pp. 305–310.
- DECOVALEX, 2023. Task B. <https://decovallex.org/D-2023/task-b.html>. (Accessed 25 May 2022).
- Donohew, A.T., Horseman, S.T., Harrington, J.F., 2000. Gas entry into unconfined clay pastes at water contents between the liquid and plastic limits. *Mineralogical Society Series*, 9. Mineralogical Society, London, UK, p. 369–394.
- Drucker, D.C., Prager, W., 1952. Soil mechanics and plastic analysis or limit design. *Q. Appl. Math.* 10, 157–165.
- Graham, C.C., Harrington, J.F., Cuss, R.J., Sellin, P., 2012. Gas migration experiments in bentonite: implications for numerical modelling. *Mineral. Mag.* 76 (8), 3279–3292.
- Guo, C., Fall, M., 2019. Modelling of preferential gas flow in heterogeneous and saturated bentonite based on phase field method. *Comput. Geotech.* 116, 103206.
- Harrington, J.F., Milodowski, A.E., Graham, C.C., Rushton, J.C., Cuss, R.J., 2012. Evidence for gas-induced pathways in clay using a nanoparticle injection technique. *Mineral. Mag.* 76 (8), 3327–3336.
- Harrington, J.F., Volckaert, G., Noy, D.J., 2014. Long-term impact of temperature on the hydraulic permeability of bentonite. *Geol. Soc. Spec. Publ.* 400 (1), 589–601.
- Horseman, S.T., Harrington, J.F., Sellin, P., 1999. Gas migration in clay barriers. *Eng. Geol.* 54, 139–149.
- Kim, K., Rutqvist, J., Harrington, J.F., Tamayo-Mas, E., Birkholzer, J.T., 2021. Discrete dilatant pathway modeling of gas migration through compacted bentonite clay. *Int. J. Rock Mech. Min. Sci.* 137, 104569.
- Kolditz, O., Bauer, S., Bilke, L., et al., 2012. OpenGeoSys: an open-source initiative for numerical simulation of thermo-hydro-mechanical/chemical (THM/C) processes in porous media. *Environ. Earth Sci.* 67 (2), 589–599.
- Kolditz, O., Nagel, T., Shao, H., Wang, W., Bauer, S., 2018. *Thermo-Hydro-Mechanical-Chemical Processes in Fractured Porous Media: Modelling and Benchmarking*. Springer International Publishing, Cham, Switzerland.
- Liu, J.-F., Skoczylas, F., Liu, J., 2014. Experimental research on water retention and gas permeability of compacted bentonite/sand mixtures. *Soils Found.* 54 (5), 1027–1038.
- Liu, J., Song, S., Cao, X., Meng, Q., Pu, H., Wang, Y., Liu, J., 2020. Determination of full-scale pore size distribution of Gaomiaozi bentonite and its permeability prediction. *J. Rock Mech. Geotech. Eng.* 12 (2), 403–413.
- Marschall, P., Horseman, S., Gimmi, T., 2005. Characterisation of gas transport properties of the opalinus clay, a potential host rock formation for radioactive waste disposal. *Oil Gas Sci. Technol.* 60 (1), 121–139.
- Mualem, Y., 1976. A new model for predicting the hydraulic conductivity of unsaturated porous media. *Water Resour. Res.* 12 (3), 513–522.
- NAGRA, 2002. *Entsorgungsnachweis für abgebrannte Brennelement, verglaste hochaktive sowie langlebige mittelaktive Abfälle*. Technical Report, No. 02–03. Nagra, Wettingen, Switzerland (in German).
- Nguyen, T.S., Le, A.D., 2015. Simultaneous gas and water flow in a damage-susceptible bedded argillaceous rock. *Can. Geotech. J.* 52 (1), 18–32.
- Ortiz, L., Volckaert, G., Mallants, D., 2002. Gas generation and migration in Boom Clay, a potential host rock formation for nuclear waste storage. *Eng. Geol.* 64, 287–296.
- Popp, T., Wiedemann, M., Böhnle, H., Minkley, W., 2007. *Untersuchungen zur Barriereintegrität im Hinblick auf das Ein-Endlager-Konzept*. Institut für Gebirgsmechanik GmbH, Leipzig, Germany (in German).
- Rawat, A., Lang, L., Baille, W., Dieudonne, A.-C., Collin, F., 2020. Coupled hydro-mechanical analysis of expansive soils: parametric identification and calibration. *J. Rock Mech. Geotech. Eng.* 12 (3), 620–629.
- Rutqvist, J., Ijiri, Y., Yamamoto, H., 2011. Implementation of the barcelona basic model into tough-flac for simulations of the geomechanical behavior of unsaturated soils. *Comput. Geosci.* 37 (6), 751–762.
- Senger, R., Enachescu, C., Doe, T., Distinguin, M., Delay, J., Frieg, B., 2006. Design and analysis of a gas threshold pressure test in a low-permeability clay formation at ANDRA's underground research laboratory, Bure (France). In: *Proceeding of TOUGH Symposium 2006*. Lawrence Berkeley National Laboratory, Berkeley, California, USA.
- Senger, R., Romero, E., Ferrari, A., Marschall, P., 2014. Characterization of gas flow through low-permeability claystone: laboratory experiments and two-phase flow analyses. *Geol. Soc. Spec. Publ.* 400 (1), 531–543.

- Senger, R., Romero, E., Marschall, P., 2018. Modeling of gas migration through low-permeability clay rock using information on pressure and deformation from fast air injection tests. *Transport Porous Media* 123, 1–17.
- Shovkun, I., Garipov, T., Tchelepi, H.A., 2020. Embedded Fracture Model for Coupled Flow and Geomechanics. ArXiv abs/2008.08064.
- Tamayo-Mas, E., Harrington, J.F., Brüning, T., Shao, H., Dagher, E.E., Lee, J., Kim, K., Rutqvist, J., Kolditz, O., Lai, S.H., Chittenden, N., Wang, Y., Damians, I.P., Olivella, S., 2021. Modelling advective gas flow in compact bentonite: lessons learnt from different numerical approaches. *Int. J. Rock Mech. Min. Sci.* 139, 104580.
- Terzaghi, K., 1936. Die Berechnung der Durchlässigkeitsziffer des Tones aus dem Verlauf der hydrodynamischen Spannungerserscheinungen. *Sitzungsber. Akad. Wiss. Wien* 132, 125–138 (in German).
- van Genuchten, M.T., 1980. A closed-form equation for predicting the hydraulic conductivity of unsaturated soils. *Soil Sci. Soc. Am. J.* 44 (5), 892–898.
- Villar, M.V., Iglesias, R.J., García-Siñeriz, J.L., 2020. State of the in situ Febex test (GTS, Switzerland) after 18 years: a heterogeneous bentonite barrier. *Environ. Geotech.* 7 (2), 147–159.
- Wang, W., Shao, H., Nagel, T., Kolditz, O., 2021. Analysis of coupled thermal-hydro-mechanical processes during small scale in situ heater experiment in Callovo-Oxfordian clay rock introducing a failure-index permeability model. *Int. J. Rock Mech. Min. Sci.* 142, 104683.
- Weetjens, E., Sillen, X., 2006. Gas generation and migration in the near field of a supercontainer-based disposal system for vitrified high-level radioactive waste. In: *Proceedings of the 11th International High-Level Radioactive Waste Management Conference (IHLRWM)*. La Grange Park, Illinois, USA, pp. 1–8.
- Wikramaratna, R.S., Goodfield, M., Rodwell, W., Nash, P.J., Agg, P.J., 1993. A Preliminary Assessment of Gas Migration from the Copper/Steel Canister. Technical Report, No. SKB-TR-93-31. Swedish Nuclear Fuel and Waste Management Co., Stockholm, Sweden.
- Wojciechowski, M., 2018. A note on the differences between Drucker-Prager and Mohr-Coulomb shear strength criteria. *Studia Geotechnica Mech.* 40 (3), 163–169.
- Xu, W.J., Shao, H., Hesser, J., Wang, W.Q., Kolditz, O., Popp, T., 2011. Simulation of dilatancy-controlled gas migration process in saturated argillaceous rock. *Computational Geomechanics, COMGEO II*. In: *Proceedings of the 2nd International Symposium, Cavtat-Dubrovnik, Croatia, 27-29 April, 2011*, pp. 693–703.
- Xu, W., Shao, H., Marschall, P., Hesser, J., Kolditz, O., 2013. Analysis of flow path around the sealing section HG-A experiment in the Mont Terri Rock Laboratory. *Environ. Earth Sci.* 70 (7), 3363–3380.
- Zhang, C.-L., 2016. The stress–strain–permeability behaviour of clay rock during damage and recompaction. *J. Rock Mech. Geotech. Eng.* 8 (1), 16–26.
- Zhu, W.C., Wei, C.H., 2011. Numerical simulation on mining-induced water inrushes related to geologic structures using a damage-based hydromechanical model. *Environ. Earth Sci.* 62, 43–54.



**Eike Radeisen** is a research fellow in the Department of Underground Space for Storage and Economic Use at the Federal Institute for Geosciences and Natural Resources (BGR) in Hannover, Germany. He graduated with a Master's degree in Geotechnical Engineering from the Technical University of Berlin, Germany. His work focuses on coupled thermo-hydro-mechanical (THM) processes in the context of radioactive waste disposal. The research is conducted within the framework of the DECOVALEX project, in which he investigates and models gas-induced fractures in claystone and bentonite. He is currently pursuing a PhD at the Technical University of Dresden, Germany.